CrystEngComm

ROYAL SOCIETY OF CHEMISTRY

PAPER

Cite this: *CrystEngComm*, 2020, **22**, 7903

Multi-dimensional architecture of Ag/α-Ag_2WO_4 crystals: insights into microstructural, morphological, and photoluminescence properties†

Lílian Cruz, *[a] Mayara M. Teixeira,[a] Vinícius Teodoro,[a] Natalia Jacomaci,[b] Letícia O. Laier,[b] Marcelo Assis,[a] Nadia G. Macedo,[c] Ana C. M. Tello,[a] Luís F. da Silva,[d] Gilmar E. Marques,[d] Maria A. Zaghete,[b] Márcio D. Teodoro[d] and Elson Longo *[a]

Received 18th June 2020,
Accepted 5th October 2020

DOI: 10.1039/d0ce00876a

rsc.li/crystengcomm

In this study, we report the potential of ethylenediamine (En) in the modification of the morphological, structural, optical and catalytic properties of α-Ag_2WO_4 crystals decorated with Ag nanoparticles (Ag NPs). Experimental techniques were used to characterize the as-synthesized samples such as X-ray diffraction, Raman, electron microscopy, X-ray photoelectron spectroscopy, X-ray absorption spectroscopy, and photoluminescence spectroscopy. The results confirmed the efficiency of En in the decoration with the formation of Ag/α-Ag_2WO_4 crystals and also the modification of α-Ag_2WO_4 morphology that indicated its influence on the crystal growth mechanism *via* self-assembly and Ostwald ripening. En affects the degree of order/disorder of the crystalline structures in long and short-ranges. In addition, photoluminescence measurements revealed a blue shift of the optical emission caused by a reduction of oxygen vacancies and an increase in structural disorder due to the En concentration used in the synthesis processes. Regarding the photocatalysis experiments, the reduction in oxygen vacancies also caused a decrease in the photoactivity of α-Ag_2WO_4 against the rhodamine B dye, thus confirming the relevance of oxygen vacancies for the development of α-Ag_2WO_4 photocatalysts.

Introduction

Material properties are determined based on various factors such as defects, particle size, morphology, crystal structure, and the combination of materials. Morphology is governed by surface anisotropic properties which, consequently, are controlled by growth and dissolution rates, wettability, surface energy, cohesion, adhesion, *etc.*[1] Several chemical synthesis methodologies have been applied to obtain compounds that exhibit distinct crystal shapes due to the direct relationship between the morphology of the materials, the physicochemical properties, and their functional applications.[2] This occurs because the morphology is directly linked to short-, medium-, and long-range crystal lattice ordering caused by the presence of reactive surfaces and the contact area, directly influencing the material properties.[3] Such factors are controlled by the synthesis methodology; therefore, it is of great importance to understand the factors that are linked to the manifestation of a specific property to develop a suitable synthesis methodology.

In addition to their efforts to control morphology, many researchers have dedicated themselves to the development of multifunctional materials, through the suitable combination of their constituents. In particular, the combination of semiconductors with metallic nanoparticles, due to the catalytic and electronic characteristics that culminate in materials with unique optical, magnetic, physicochemical, catalytic, and plasmonic properties. Silver-containing materials have been widely studied, due to their several applications, such as in antibacterial[4,5] materials, bioimaging,[6] sensors,[7] heterogeneous catalysis,[8–10] and optics.[11–13] As can be found in the work conducted by

[a] *Center of Development of Functional Materials, Federal University of São Carlos, Rod. Washington Luiz, km 235, 13565-905, São Carlos, SP, Brazil. E-mail: elson.liec@gmail.com*
[b] *Interdisciplinary laboratory of ceramic studies, São Paulo State University, 14800-900, Araraquara, SP, Brazil*
[c] *Department of Physical Chemistry, Institute of Chemistry, State University of Campinas, 13083-970, Campinas, SP, Brazil*
[d] *Department of Physics, Federal University of São Carlos, Rod. Washington Luiz, km 235, 13565-905, São Carlos, SP, Brazil*

† Electronic supplementary information (ESI) available: Results of the refinement by the Rietveld method and measures of the deviations at the binding angles, vibrational modes (Raman), TEM images. See DOI: 10.1039/d0ce00876a

Barreca *et al.*,[12] silica-supported silver nanoparticles were obtained by radio frequency (rf) sputtering from Ar plasma, under soft conditions. The authors observed modifications in the optical properties of the material, such as increased absorption in the visible region, due to surface-plasmon resonance, widening of the band due to the increase in particle size and shape distribution, in addition to the red effect, caused by the particle coalescence. On another occasion, Barreca *et al.*[13] used the same rf-sputtering method to prepare Ag–Au alloys supported on silica. They analyzed the control of the size, shape, structure, and dispersion of the particles and concluded that the control of reaction conditions and thermal treatment function makes it possible to fine-tune the optical properties.

Our research group has studied the silver tungstate (α-Ag_2WO_4) compound synthesized by different methodologies.[14,15] Significant interest in α-Ag_2WO_4 has recently developed because it presents interesting applications for sensors,[16] light-emitting diodes (LEDs),[17] degradation of organic contaminants,[18] and inhibition/destruction of pathogenic microorganisms.[19] These applications depend on the method utilized to obtain the α-Ag_2WO_4 compound. Different methodologies have been used to synthesize α-Ag_2WO_4, such as coprecipitation (CP),[16] the conventional hydrothermal (CH)[20] method, the microemulsion method,[11] and the microwave-assisted hydrothermal (MAH)[21] method, among others.

To get decorated semiconductors, Koyappayil *et al.* synthesized Ag@Ag_2WO_4 nanorods *via* the hydrothermal route, using cetyltrimethylammonium bromide (CTAB) in the reaction medium. They observed an excellent ability to detect hydrogen peroxide and glucose.[7] Meanwhile, Liu *et al.* obtained Ag_2WO_4 nanowires decorated with Ag NPs, but by the hydrothermal method followed by the chemical reduction process, verifying good semiconductor stability and improvement of the photoactivity in the visible region due to the high production of OH* radicals and the effects of plasmon resonance of the surface.[22] Although these works present simple methodologies for the preparation of Ag/Ag_2WO_4 crystals, few simple methods promote a suitable control of the morphological and structural properties of the semiconductor decorated with (or without) Ag NPs.

Recently, the modifier En has gained attention due to its bidentate complexing properties, which include high polarity, high chelating power, alkalinity, and the ability to act as a reducing agent.[23] In this study, we analyzed the synthesis of α-Ag_2WO_4 *via* the MAH method with two concentrations of the complexing agent, En, investigating its influence on short-, medium-, and long-range ordering, morphology, optical, and photocatalytic properties.

Also, the formation of Ag NPs on the surface of α-Ag_2WO_4 was verified due to the use of En in the synthesis, without additional processes. This manuscript addresses a strategy for obtaining multidimensional and functionalized architectures with metallic nanoparticles and also provides an understanding of the factors that fine-tune the optical and photocatalytic properties of α-Ag_2WO_4.

Experimental section

Preparation of Ag/α-Ag_2WO_4 crystals

In two separate beakers, a solution of 0.5 mmol of En ($C_2H_8N_2$, 99.8%, Sigma-Aldrich) and 2 mmol of silver nitrate ($AgNO_3$, 99.8%, Cennabras), dissolved in 10 mL of deionized water at room temperature, was prepared. Then, an $AgNO_3$ solution was added to the En solution and was continuously stirred for 1 h, yielding a brown suspension, which, after 15 min, turned black. Separately, 1 mmol of sodium tungstate ($Na_2WO_4{\cdot}2H_2O$, 99%, Stream Chemicals) was dissolved in 80 mL of deionized water, which was added to the mixture containing En and $AgNO_3$, resulting in an instantly formed white precipitate. This solution was continuously stirred for 10 min. The same procedure was followed for the second sample using 1 mmol instead of 0.5 mmol of En. The suspension obtained was transferred to a Teflon vessel (100 mL) and then treated in an MAH reactor at 160 °C for 32 min. The resultant black powder was centrifuged 3 times with acetone, 3 times with ethyl alcohol, 4 times with distilled water, and then dried at 60 °C for 12 h. The variations of the reaction conditions are shown in Table 1. For the synthesis without En, the procedure was the same except $AgNO_3$ was dissolved in 20 mL of deionized water, and the powder obtained exhibited a light pink color. The samples were named W for the sample without En and WE0.25 and WE0.5 for the En/Ag^+ ratios of 0.25 and 0.50, respectively.

To investigate the growth and formation of the morphology, the WE0.25 and WE0.5 syntheses were performed for the following time durations: 2, 4, 8, and 16 min. The 5 min time duration in WE0.5 was added because of a morphological change observed between 4 and 8 min.

Photocatalytic measurements

The photocatalytic activity of the as-synthesized samples was probed by quantifying the removal of rhodamine B (RhB; 95%, Mallinckrodt) dye in aqueous solution under UV irradiation. The samples (50 mg) were immersed in 50 mL of RhB solution (1×10^{-5} mol L^{-1}). Before illumination, the suspensions were sonicated for 5 min in an ultrasonic bath (Branson, model 1510; frequency 42 kHz), then stored in the dark for 30 min to allow for saturated adsorption of RhB onto the catalyst. The beaker was then placed in a photoreactor kept at 20 °C and illuminated by six UV lamps (TUV Phillips, 15 W, and maximum intensity of 254 nm). At 5 and 15 min intervals, an aliquot of 0.5 mL was removed and then centrifuged at 10 000 rpm for 2 min to remove the sample from the suspension. Finally, the removal of dye was monitored using a spectrometer (Jasco V-660) to measure, at 554 nm, the intensity of the RhB characteristic absorption peak.

Computational methods

The polyhedron energy, E_{poly}, was calculated using eqn (1), and the energy profile, which allows the connection of the

Table 1 Identification of α-Ag_2WO_4 samples and variation of reaction conditions

Samples	n, mmol WO_4^{2-}	n, mmol Ag^+	n, mmol En*	En*/Ag^+	[En*], mmol L^{-1}
W	1.0	2.0	0	0	0
WE0.25	1.0	2.0	0.5	0.25	5.0
WE0.5	1.0	2.0	1.0	0.50	10.0

En*: ethylenediamine.

ideal morphology with the final experimental morphology, was constructed.

$$E_{poly} = \sum C_i \cdot E_{surf}^{(hkl)} \quad (1)$$

where C_i is the percent contribution of the surface area to the total area of a polyhedron ($C_i = A^{(hkl)}/A^{(poly)}$) and $E_{surf}^{(hkl)}$ is the surface energy.[24]

Characterization techniques

The X-ray powder diffraction technique (XRD) was employed to evaluate the crystalline structure in the long-range, the composition phase and the lattice parameters of the sample Ag/α-Ag_2WO_4, using a diffractometer (Shimadzu, model XRD 6000) with Cu-K_α radiation (λ = 1.5406 Å) in the 2θ range from 5° to 110° with a step of 0.02° and a scanning speed of 0.2° min^{-1}. The Rietveld refinement method was employed to verify the bond angle, the quantitative analysis phase, and the lattice parameters.[25] Refinement calculations were performed using TOPAS Academic (v.5.4) software. The parameters refined were the scale factor, background (polynomial 6 terms), sample shift, crystal lattice, anisotropic peak broadening, preferential orientation, and isotropic thermal parameters. The background was corrected by the Chebyshev function with a polynomial of 10 terms. The peak profile was modeled by Finger *et al.*,[26] a function for the correction of peak asymmetry due to axial divergence. The anisotropic broadening of the sample was modeled using Stephens's model.[27] The weight fraction W_α of the crystalline phases present in the heterostructure Ag/α-Ag_2WO_4 is estimated using Hill and Howard's[28] relationship:

$$W_\alpha = \frac{S_\alpha (ZMV)_\alpha}{\sum_{i-1}^{n} S_i (ZMV)_\alpha} \quad (2)$$

where n, S, Z, M and V are the number-phase in the sample, the scale factor, the number of formula units per unit cell, the mass of the formula unit and the unit-cell volume, respectively. Since all the phases are crystalline in the sample, α is the j value for a specific phase (Ag or Ag_2WO_4) among the total phase in the heterostructure.[28] In other words, the amount phase is relative and not absolute; for this reason, the structural quality of the sample in refinement is fundamental.

The structural quality and the performance of the calculation are guaranteed by R_{wp}, which is the percentage difference of the calculated intensity observed point by point; R_{exp}, which is the best statistically expected value for R_{wp}; Gof^2 (goodness of fit), which represents the ratio between R_{wp} and R_{exp}; and R_{Bragg}, which indicates the quality of the refined structural model and also the good visual agreement between the adjustments made.[25,29]

The morphological properties were analyzed using field emission scanning electron microscopy, FE-SEM (Philips-FEI-Inspect F50) and transmission electron microscopy, TEM (FEI-Tecnai G2 F20 operating at 200 kV). High-resolution transmission electron microscopy (HRTEM) measurements were performed to investigate the planes and assign them to the possible phases present in the as-synthesized samples.

Raman spectra were collected using an Ar ion laser (Horiba Jobin-Yvon iHR550, λ = 514.5 nm, 20 mW) as an excitation source, with a scanning range from 50 to 1100 cm^{-1}. Room-temperature photoluminescence (PL) measurements were performed using a 355 nm laser (Cobol/Zouk) as an excitation source focused on a 200 μm spot with a constant power of 5 mW. The luminescence signal was dispersed by a 19.3 cm spectrometer (Andor/Kymera) and detected by a Si charge-coupled device (Andor/Idus BU2).

The electronic and local atomic structures around the tungsten atoms were probed using X-ray absorption near-edge structure (XANES). The W-L edge XANES spectra of the α-Ag_2WO_4 samples were collected at the XAFS2 beamline at the Brazilian Synchrotron Light Laboratory (LNLS). The XANES spectra were collected at the W-L1 edge in a transmission mode at room temperature. The spectra were recorded using energy steps of 1.0 eV before and after the edge, and 0.7 and 0.9 eV near the edge-region for the L1 edge. For the XANES analysis, the background was removed from all the spectra, and normalized using as the unit of measurement the first extended X-ray absorption fine structure (EXAFS) oscillation, using MAX software.[32] The X-ray photoelectron spectroscopy, XPS, measurements were made using a Scienta Omicron ESCA+ with a monochromatic X-ray source (Al Kα, $h\nu$ = 1486.7 eV). Peak deconvolution was performed using a Voigt line shape with a Shirley nonlinear sigmoid-type baseline and all binding energies were calibrated with reference to the surface adventitious C 1s peak at 284.8 eV as an internal standard.

Results and discussion

XRD and Rietveld refinement analysis

Fig. 1 shows the XRD patterns of the α-Ag_2WO_4 powder prepared by the MAH method. The orthorhombic structure was

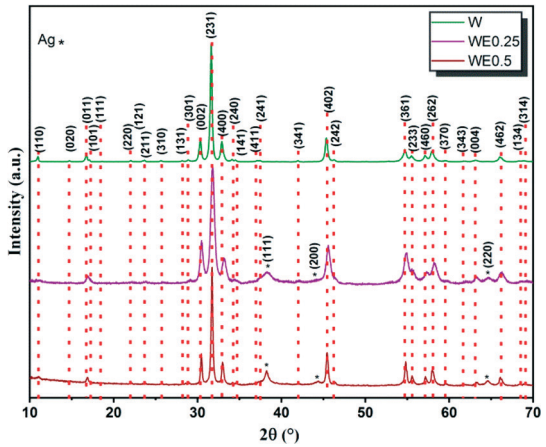

Fig. 1 XRD patterns of the α-Ag_2WO_4 samples synthesized by the MAH method.

confirmed in all patterns associated with α-Ag_2WO_4 (space group *Pn*2*n*), according to Inorganic Crystal Structure Database (ICSD) card no. 4165.[3,30,33] The WE0.25 and WE0.5 samples also showed reflections at 38.20°, 44.40°, and 64.60°, which were indexed to crystallographic planes (111), (200), and (220), related to the cubic structure of metallic Ag (ICSD, card no. 64997).[31,34] The lattice parameters of the samples estimated from the Rietveld refinement are presented in Table 2. As can be seen, the results are similar to those reported in previous studies,[30] and no significant variation between the samples was found. Furthermore, as a result of the use of En in the synthesis procedure, we observed the presence of two crystalline phases: α-Ag_2WO_4 and metallic Ag.

The obtained cell volumes of the W, WE0.25, and WE0.5 samples were 767.5, 772.0, and 771.1 $Å^3$, respectively, which differ from each other and are smaller than that previously reported by Skarstad *et al.*,[30] *i.e.*, a cell volume of 775.56 $Å^3$. The cell volume contraction is related to the synthesis method utilized. The CH method reported by Skarstad *et al.*[30] is similar to the method employed here. However, compared to the MAH method, the CH method employs lower heating rates, which influences the speed of crystallization and nucleation. The MAH method uses a high-heating rate, which causes atomic stacking of the crystalline structure, promoting the formation of vacancies, which culminates in shrinkage of the complex unit cell. However, the samples that were obtained with En showed an expansion of the unit cell concerning the pristine sample caused by the complexing agent acting on the synthesis control, which also decreases the nucleation rate. In the WE0.25 and WE0.5 samples, beyond the α-Ag_2WO_4 phase, a secondary phase related to metallic Ag (Ag^0) was found. Its lattice parameters are similar to values reported in previous studies, *i.e.*, *a* = 4.08 Å (ICSD card no. 64997).[31,34] As shown in Table 2, the quantitative phase analysis of the WE0.25 and WE0.5 samples presented approximately 19% and 31% of metallic Ag. As previously mentioned, the formation of metallic Ag is related to En. Additionally, the WE0.5 sample exhibited a significant increase in the Ag content compared to the WE0.25 sample, suggesting that the concentration of En also influences the amount of metallic Ag in the sample.

The unit cell illustrated in Scheme 1 represents the arrangement of [AgO_y] (*y* = 2, 4, 6, and 7) and [WO_6] constituent clusters of α-Ag_2WO_4. This unit cell was constructed from the lattice parameters and atomic coordinates obtained by the Rietveld refinement utilizing the Visualization for Electronic and Structural Analysis (VESTA) software.[35] The [AgO_y] (*y* = 2, 4, 6, and 7) clusters have distorted angles and different coordination numbers, and the W clusters are coordinated by six oxygen atoms and also have distorted angles.

It can be observed from Scheme 2 that the O–Ag–O and O–W–O bond angles of the W and WE0.5 samples present greater deviations compared to the angles in the reference clusters,[30,33] following the order WE0.25 < W < WE0.5. As can be seen, the addition of En caused structural organization up to the limit, causing more significant structural disorders than those observed for sample W. The increase in the En concentration then caused a local organization in the Ag–O and W–O bonds, and the distortion of these bonds in the WE0.25 and WE0.5 samples, respectively.

XPS analysis

These measurements were performed to verify the chemical composition and oxidation states of the constituent elements on the surface of the samples. Fig. 2(a) displays the survey spectra, where it is possible to observe the presence of the

Table 2 Lattice parameters and unit cell volumes obtained by Rietveld refinement for the α-Ag_2WO_4 samples

				Samples		
			Ref.	W	WE0.25	WE0.5
α-Ag_2WO_4	L P (Å)	*a*	10.89(2)[30]	10.8707(4)	10.876(2)	10.892(1)
		b	12.03(2)[30]	11.9931(5)	12.038(3)	12.018(2)
		c	5.92(2)[30]	5.8865(3)	5.902(1)	5.8909(9)
	V ($Å^3$)		775.56(*)[30]	767.45(6)	772.0(3)	771.1(2)
	Content (%)		100	100	81(1)	69.3(9)
Ag^0	L P (Å)	*a*	4.07724(4)[31]	—	4.086(1)	4.0865(7)
	V ($Å^3$)		67.78(*)[31]	—	68.26(7)	68.24(3)
	Content (%)		100	0	18.(1)	30.6(9)

L P: lattice parameters (*) not indicated in the cif.

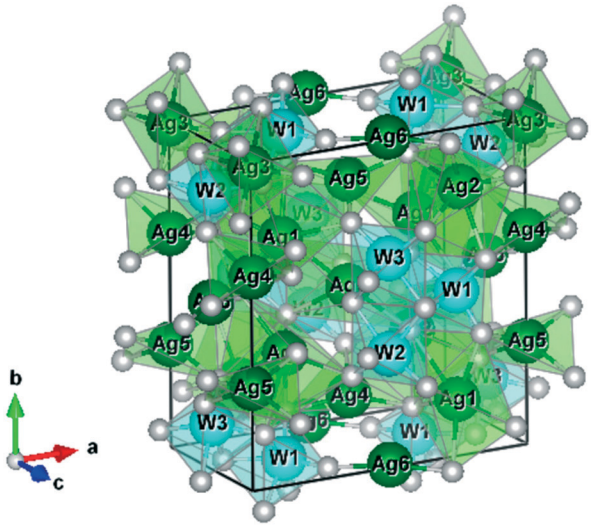

Scheme 1 Schematic representation of the crystalline unit cell of α-Ag_2WO_4 (bulk).

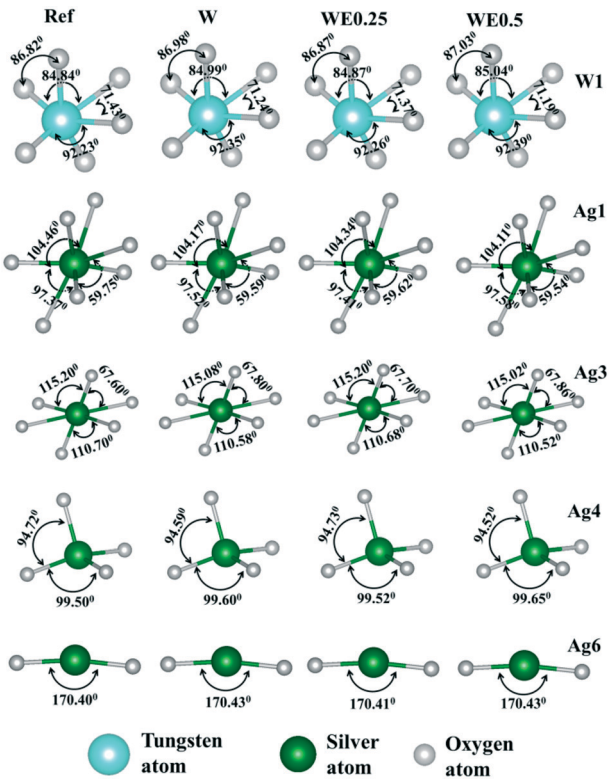

Scheme 2 Schematic representation of the angular deviation of [AgO_y] (y = 2, 4, 6 and 7) and [WO_6] clusters.

elements Ag, W, and O in the samples. The presence of extra elements was not identified, suggesting that the syntheses employed were successful. Note that the presence of C is inherent to the equipment and was observed in all the samples.

The high-resolution XPS spectra of the Ag 3d region of the W, WE0.25, and WE0.5 samples were assigned to the doublets, $3d_{3/2}$ and $3d_{5/2}$, due to the spin–orbit coupling, as shown in Fig. 2(b). These peaks can be deconvolved into two peaks that correspond to metallic silver and ionic silver. However, as there is an overlap between deconvolved peaks, it is recommended to measure the Auger parameter, since it confirms the presence of different oxidation states.[12] The Auger parameter was calculated by the sum of the binding energy of Ag 3d and the kinetic energy of Auger MNN (KE) (= BE ($Ag3d_{5/2}$) + KE (Auger ($M_4N_{45}N_{45}$)) (characteristic energy, eV)).[36] By amplifying the survey in the Auger Ag $M_4N_{45}N_{45}$ region, the graph shown in Fig. 2(c) was obtained. The Auger parameter values obtained for W, WE0.25, and WE0.50 samples were 724.08, 724.46, and 724.83 eV. Since the Auger parameter for ionic silver is 724.0 eV and for metallic silver is 726.0 eV, such findings indicate the presence of a mixture of silver species exhibiting different oxidation states.[37] It was again observed that the concentration of En in the syntheses favored the formation of metallic Ag on the α-Ag_2WO_4 surface, because the increase in the proportion of the complexing agent modified the proportion of Ag species on the surface of the particles.

Furthermore, the high-resolution XPS spectra in the O 1s region, shown in Fig. 2(d), were deconvoluted into two peaks. The peak at approximately 529.9 eV refers to lattice oxygen; the other peak at approximately 531.4 eV is characteristic of oxygen vacancies.[38,39] It is noted that the sample WE0.5 showed a considerable reduction in oxygen vacancies. This behavior can be linked to the increase in the percentage of metallic Ag found by the XRD refinement analyses. As illustrated in Fig. 2(e), the high-resolution XPS spectra in the W4f region show two peaks at approximately 34.7 eV and 36.8 eV, which are associated with $W4f_{7/2}$ and $W4f_{5/2}$, referring to the 6+ oxidation state of W.[40,41]

XANES analysis

This spectroscopy technique was used to obtain information of the local structure around the W atoms in the α-Ag_2WO_4 samples. Fig. 3(a) shows the W LI-edge XANES spectra of α-Ag_2WO_4. Fig. 3(b) displays the W LI-edge XANES spectra of the α-Ag_2WO_4 samples and the following references, WO_2, m-WO_3, and Na_2WO_4. From Fig. 3(a) it can be observed that the spectra present similar characteristics (pre- and post-edge regions), indicating that the samples have a similar local structure. Moreover, the addition of En did not affect the environment around the W atoms. Since the local structures of the α-Ag_2WO_4 samples are similar, we compared only the spectrum of the WE0.5 sample with reference standards (WO_2, m-WO_3, and Na_2WO_4), as seen in Fig. 3(b). From this figure, we observed a difference in the spectra, particularly in the pre-edge region, where P1 is located, which is known to be sensitive to the local symmetry of the absorber atoms.[42,43] We verified that the WE0.5 spectrum is similar to the spectrum of the m-WO_3 reference, which means that these compounds have similar local symmetry.

According to the literature, the physical origin of the P1 peak is an electronic transition from 2s(W) → 5d(W) + 2p(O).[42,44] The transitions originating at the pre-edge peak

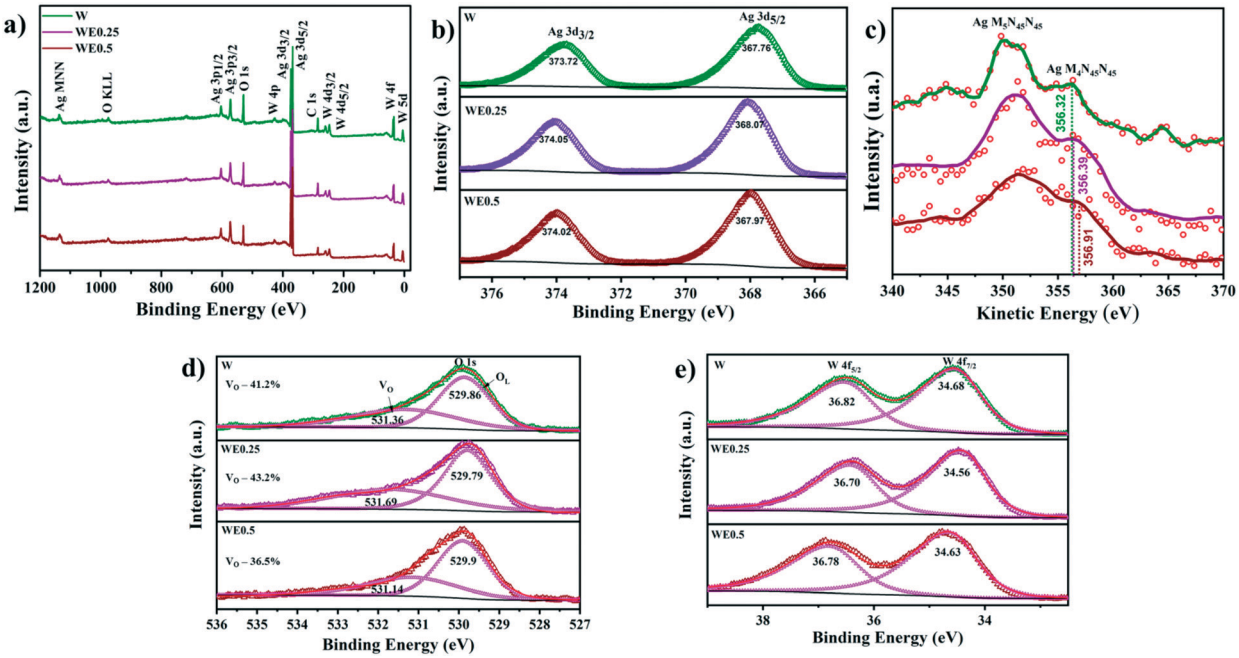

Fig. 2 XPS spectra of the α-Ag_2WO_4 samples. (a) Survey spectra, b) Ag 3d, c) $AgM_4N_{45}N_{45}$ auger, d) O 1s and e) W 4f core level spectra.

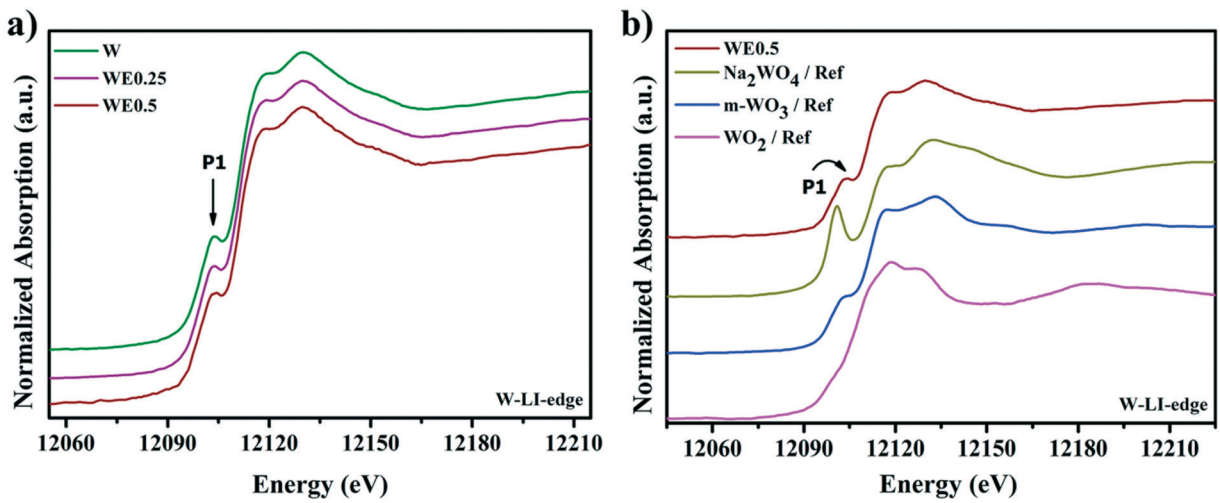

Fig. 3 a) W-LI edge XANES spectra of the α-Ag_2WO_4 samples and b) XANES spectra of the WE0.5 sample and the reference samples (Na_2WO_4, *m*-WO_3 and WO_2).

are not allowed for regular octahedral symmetries (WO_6), but are allowed for distorted octahedral structures (WO_6).[44,45] The spectrum of a compound exhibiting units with regular octahedral symmetry will not present a pre-peak, whereas units with distorted octahedral symmetry will have a small pre-edge peak, and units with tetrahedral symmetry will show an intense pre-peak in the XANES spectrum.[45]

Fig. 3(b) shows that the intensity of the P1 peak is higher for the Na_2WO_4 compound where W atoms exhibit regular tetrahedral coordination, *i.e.*, WO_4 units. However, a shoulder can be observed for the *m*-WO_3 reference and WE0.5 sample. Note that the pre-peak P1 is absent in compounds presenting regular WO_6 units; however, distortions in the octahedral symmetry are indicated by a shoulder in the pre-edge region, as presented in Fig. 3(b). Therefore, the XANES analyses revealed that the α-Ag_2WO_4 samples are formed by distorted octahedral WO_6 clusters.

Raman spectroscopy

Structural order–disorder in a short-range can be analyzed by Raman spectroscopy. The micro-Raman spectra of the as-obtained samples are presented in Fig. 4. These spectra show the α-Ag_2WO_4 vibrational modes in the range of 50 to 1100 cm^{-1}. The bands observed below 500 cm^{-1} are characteristic of the vibrational modes between silver clusters [AgO_y] (y = 7,

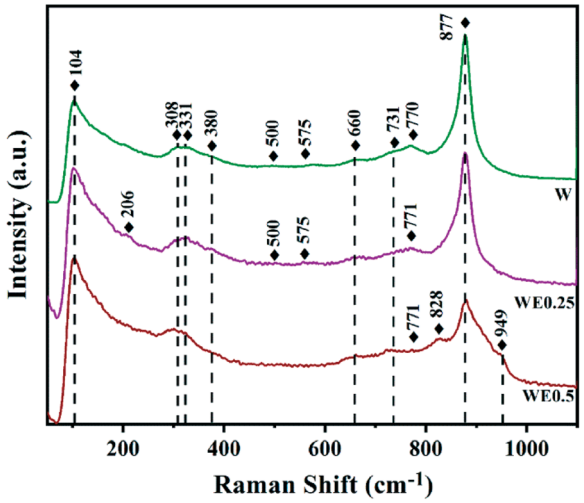

Fig. 4 Raman spectra of the α-Ag_2WO_4 samples synthesized *via* the MAH method.

6, 4, and 2) and between Ag^+ and WO_4^{2-} ions in the Ag–O–W bond, known as external vibrational modes. Otherwise, the bands identified above 500 cm^{-1} are associated with internal vibrational modes and are derived from tungsten clusters [WO_6]. Thus, the most intense bands at 96 cm^{-1} and 871 cm^{-1} come from the symmetrical stretching of the [AgO_y] and [WO_6] clusters, respectively.[46,47]

All the spectra presented in Fig. 4 show the modes obtained by theoretical calculations with some position deviations, which, according to the literature, are caused by different factors such as synthesis conditions, distortions of O–Ag–O or O–W–O bonds, interaction between ions, and average crystallite size.[21,48] The W and WE0.25 samples showed similar Raman spectra, indicating that the En concentration used to synthesize the WE0.25 sample did not influence the ordering in a short-range of α-Ag_2WO_4.

In addition to the expected theoretical modes, the WE0.5 sample presents 2 weak bands centered at 828 and 949 cm^{-1}, which are attributed to the WO_4^{2-} unit due to the stretch and bend deformations.[33,49] This finding suggests that the use of high En concentrations is able to display vibrational modes that do not appear generally due to low intensity, and it is possible to observe the mode widening at 828 cm^{-1}, which indicates that the α-Ag_2WO_4 structure was disrupted at short distances.[33,49]

Morphological properties

Fig. 5 shows the FE-SEM images of the as-synthesized α-Ag_2WO_4 samples. It can be observed that the W sample exhibits a morphology similar to microrods, Fig. 5(a), which is the most stable morphology for this material synthesized in an aqueous medium, as previously reported.[15] The microrods obtained for the W sample had an average length of 2.12 ± 0.13 μm and an average width of 0.26 ± 0.01 μm, as presented in Fig. 6(a).

In Fig. 5(b), nanorods organized in hollow microflowers and decorated with nanoparticles (NPs) are observed for the WE0.25 sample. The hollow microflowers (WE0.25) have an average width of 0.63 ± 0.01 μm, consisting of nanorods and NPs with an average width and diameter of 33.8 ± 0.6 nm and 13.8 ± 0.2 nm, respectively, as presented in Fig. 6(b). The micrograph of the WE0.5 sample, Fig. 5(c), shows microrods organized in solid microflower structures also decorated with NPs. The solid microflowers (WE0.5) have a diameter of 2.41 ± 0.03 μm and are composed of microrods with an average length of 0.88 ± 0.01 μm and an average width of 0.12 ± 0.01 μm, decorated with NPs with an average diameter of 25.0 ± 0.2 nm, as observed in Fig. 6(c). Furthermore, it was verified that the concentration of En governs the achievement of nanorods or microrods, and hollow or solid microflowers.

Fig. 7 shows the HR-TEM image with the corresponding interplanar distances of the particles that decorated the WE0.25 sample, which is a composite of α-Ag_2WO_4 and Ag NPs, and presents a very stable behavior under the TEM electron beam. Crystal planes (411), (132), and (211) were identified, whose interplanar distances were 2.49 Å, 2.35 Å, and (3.83 Å and 3.75 Å), respectively (Fig. 7(b–e)). These planes can be assigned to the α-Ag_2WO_4 orthorhombic structure (ICSD, card no. 4165).[30,33]

In addition, the interplanar distances were measured to be 2.42 Å and 2.47 Å (Fig. 7(f and g)), and can be indexed to the (111) family of planes in metallic Ag with a cubic

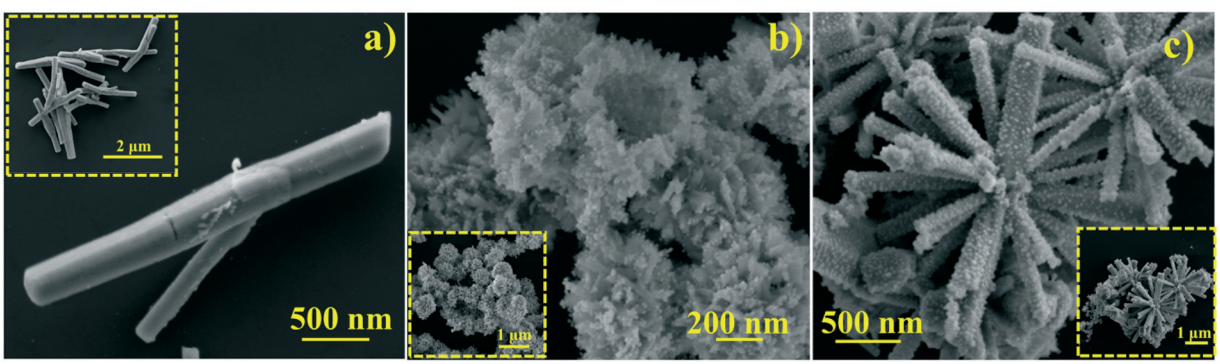

Fig. 5 FE-SEM micrographs of the α-Ag_2WO_4 microcrystals synthesized *via* the MAH method. The insets show the FE-SEM images at low magnifications. a) W, b) WE0.25 and c) WE0.5.

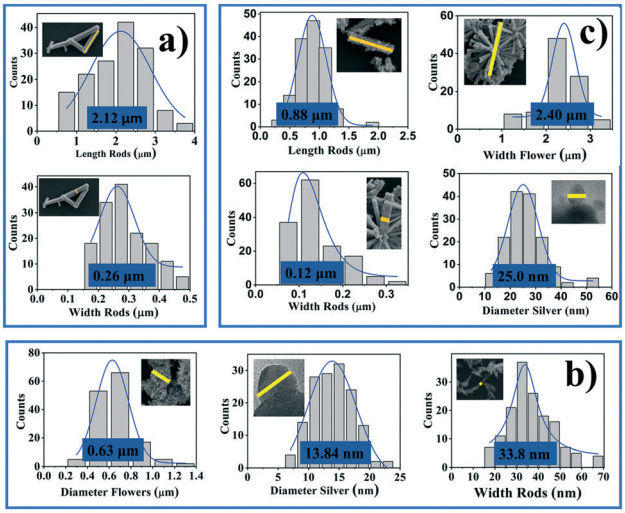

Fig. 6 Distribution of the α-Ag_2WO_4 particle sizes: a) W, b) WE0.25 and c) WE0.5.

structure (ICSD card no. 64997).[31,34] Therefore, it is possible to conclude that the NPs that decorate the WE0.25 and WE0.5 samples are Ag metallic NPs.

Growth mechanism

In the absence of En, the Ag^+ and WO_4^{2-} ions precipitate as α-Ag_2WO_4, leading to preferential surface growth (010) and microrod formation, as presented in Fig. 5(a). A morphological change was observed by introducing En to the synthesis, due to the formation of the Ag(I)complex (see eqn (3) and (4)). To understand how the hierarchical formation of the structures occurred, a time-dependent experiment was performed and the intermediate products were analyzed. The FE-SEM images of the intermediates from different reaction times are shown in Scheme 3. In the first 4 min of MAH synthesis of the WE0.25 sample, rod agglomerates were observed. After 8 min of MAH treatment, they self-organized into hierarchical solid microflowers and, after 16 min of MAH treatment, these structures evolved into hierarchical hollow structures (see Scheme 3(a)). For the synthesis of the WE0.5 sample, in the first 4 min of the reaction, polyhedron agglomerates are observed, which after 5 min solubilize, recrystallize, and self-organize into an unfinished solid. Then, after 16 min of MAH treatment, well-defined rods and hierarchical solid microflowers are observed, as shown in Scheme 3b.

$$\mathrm{Ag(I)} + \mathrm{complex} \underset{K_f}{\rightarrow} \mathrm{Ag(I)complex} \quad (3)$$

$$\mathrm{Ag(I)complex} \underset{K_f^{-1}}{\rightarrow} \mathrm{Ag(I)} + \mathrm{complex} \quad (4)$$

$$\mathrm{Ag(I)complex} \rightarrow \mathrm{Ag(0)} + \mathrm{complex(I)} \quad (5)$$

When $K_f = 5.01 \times 10^7$ and $K_f^{-1} = 1.99 \times 10^{-8}$.

An analogous process was discussed by Ding *et al.*[50] in the synthesis of $CeVO_4$ *via* the conventional hydrothermal route using L-aspartic acid (L-Asp) as a capping and complexing agent. These researchers concluded that the formation of hollow or solid beads of $CeVO_4$ depends on the presence and amount of L-Asp used. From their observations, they suggested that the particles grow according to the Ostwald ripening mechanism and that the morphology is defined by the self-assembly process. According to Ding *et al.*, L-Asp influenced the solubility of the particles present inside the newly formed $CeVO_4$ spheres, which reprecipitated on the outer particles, forming larger particles and hollow microspheres, by the Ostwald ripening process. In addition, L-Asp can be selectively adsorbed to different surfaces, causing different growth rates, which results in cubic structures, and directs the organization of these cubes into spheres, a phenomenon known as self-assembly. This mechanism can be extended to the case of α-Ag_2WO_4, where

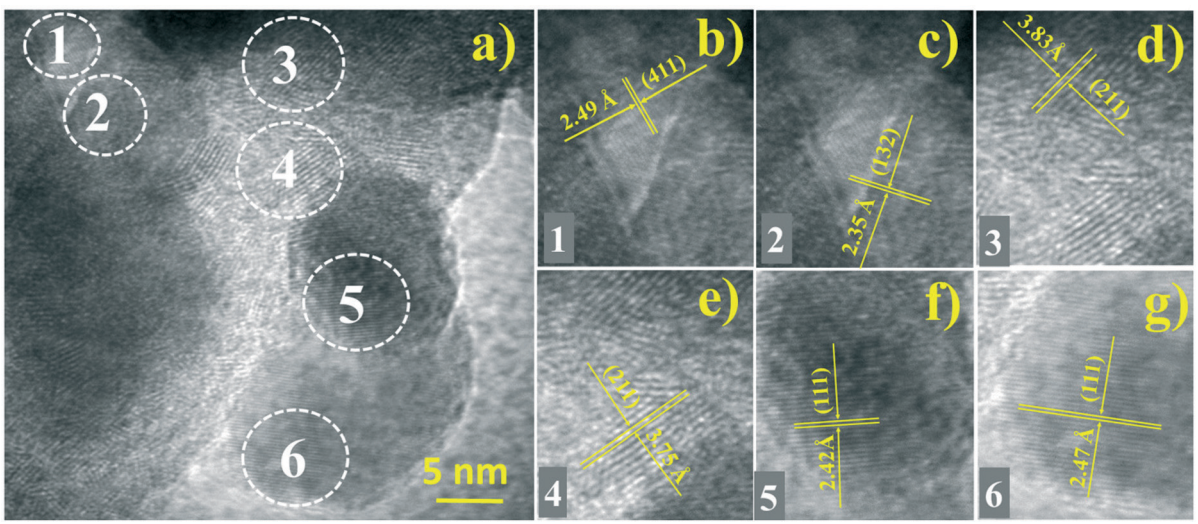

Fig. 7 HR-TEM image of the a) WE0.25 sample and magnified regions corresponding to α-Ag_2WO_4 (b–e) and to Ag NPs (f and g).

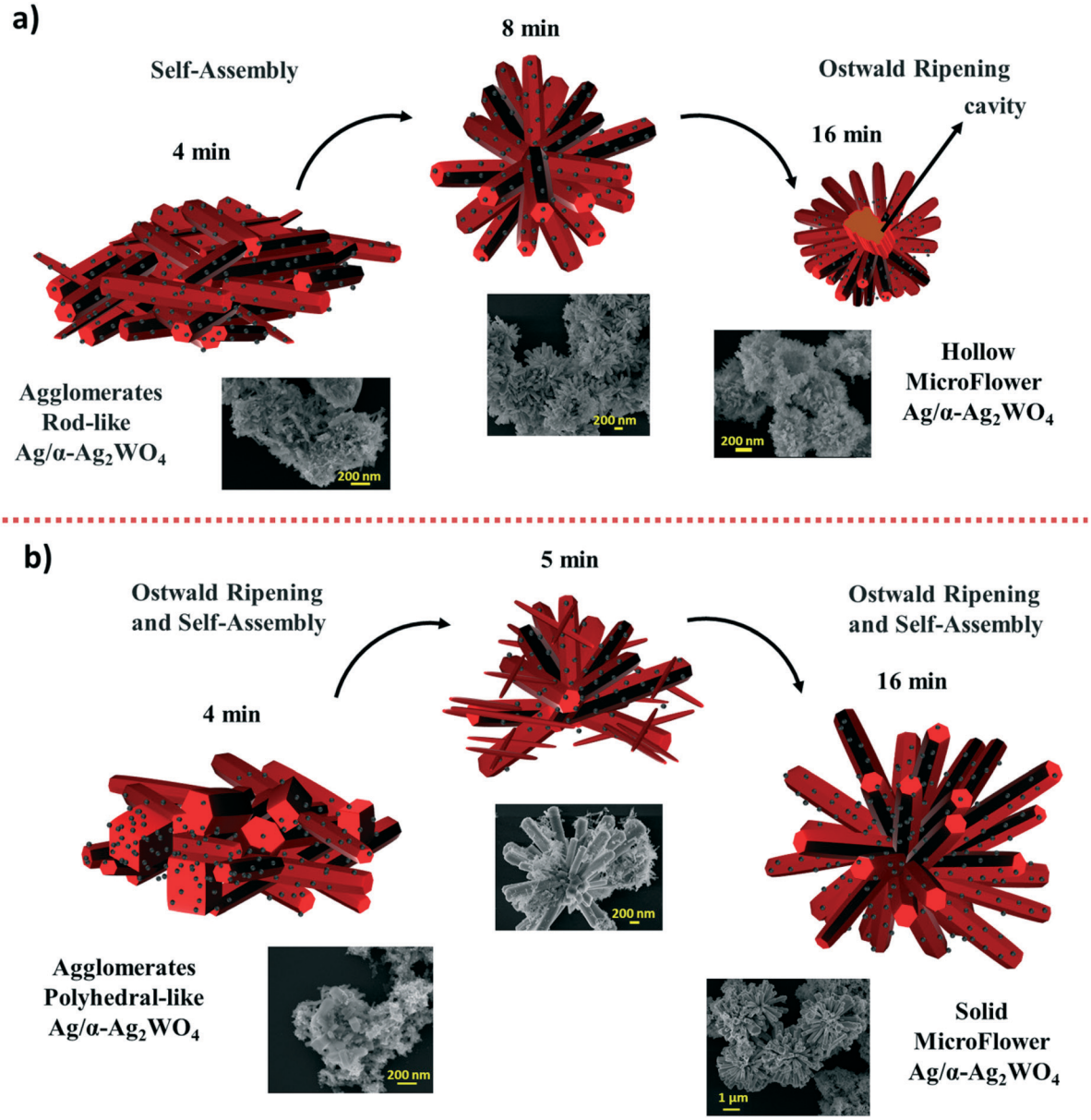

Scheme 3 Schematic illustration of the proposed growth mechanism leading to the formation of α-Ag_2WO_4 samples: a) WE0.25 and b) WE0.5.

the En acts as L-Asp, resulting in new morphologies through self-assembly and Ostwald ripening.

Scheme 3 illustrates the growth mechanism proposed for the WE0.25 and WE0.5 samples. Based on the above discussion, the formation of the morphology for the WE0.25 sample was proposed to proceed by self-assembly followed by the Ostwald ripening process, as presented in Scheme 3(a). The model proposes that addition of En influences the solubility of the small and less crystallized particles present inside the newly formed microflower α-Ag_2WO_4, which reprecipitated on the outer, larger and more crystallized particles, forming larger particles and hollow structures, in addition to guiding the organization of nanorods and forming the hollow microflower, as shown in Fig. 5(b).[51] However, as depicted in Scheme 3(b), by increasing the concentration of En in the reaction medium, a solid, not a hollow structure, was observed. It is suggested that, during the formation of the solid microflower, the redissolution of α-Ag_2WO_4 occurs from the smaller external particles, different from the sample WE0.25 in which redissolution occurs from the internal particles, as we observed in Scheme 3(b), in the image referring to the 5 min mark, where we see nanorods recrystallizing over the pre-existing microrods. In this way, we obtained particles with diameters and lengths greater than the rods that constitute the WE0.25 sample, as a result of the Ostwald ripening process. We also observed that the particles are recrystallized, organized, and oriented by En, as proposed by Ding *et al.*,[50] by the self-assembly mechanism. Therefore, to obtain the WE0.5 sample, it was proposed that the Ostwald ripening and self-assembly mechanisms occur at the same time.

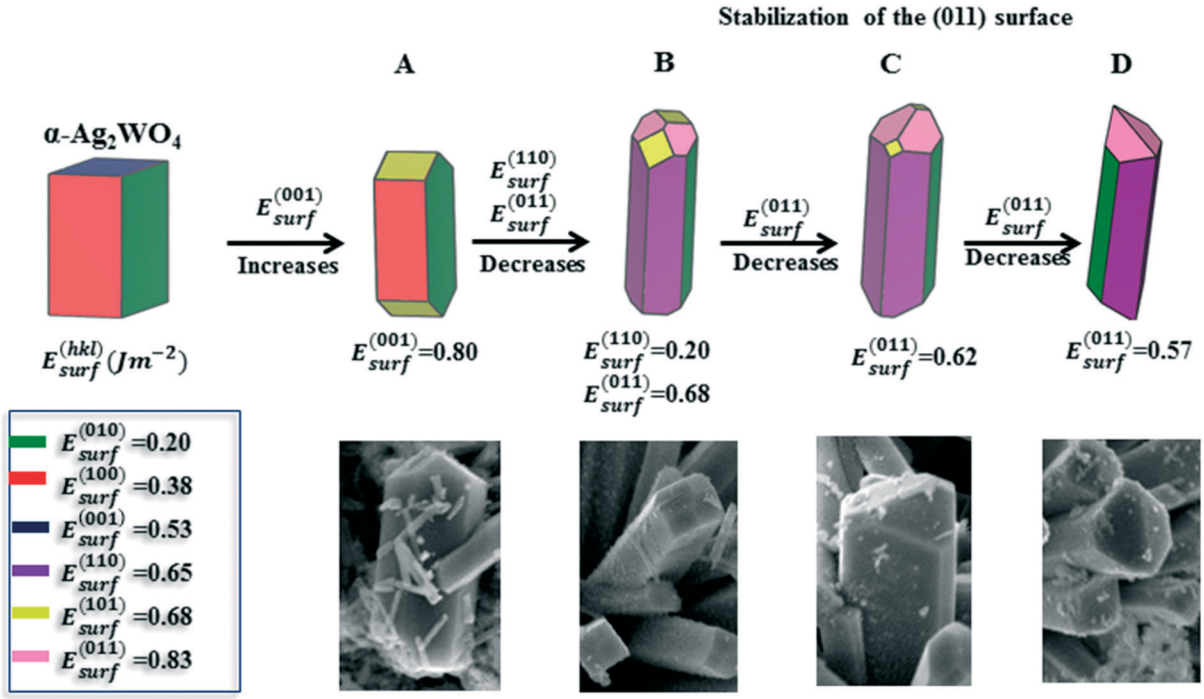

Scheme 4 Crystallographic structure and morphologies of the WE0.5 sample, with crystal planes (101), (100), (001), (110), (010), and (011). Surface energy is in J m^{-2}. Experimental FE-SEM images of the WE0.5 samples obtained at different times of the MAH method are included for comparison.

Concomitant to the Ag^{+} ion complexation and particle growth orientation processes, En reduces Ag^{+} ions (eqn (5)) and consequently, decorates the nanorods and microrods of the WE0.25 and WE0.5 samples with Ag NPs, respectively. Wang *et al.* used En to obtain copper crystals exhibiting different morphologies. To attain this objective, they modified the conditions in the synthesis methodology, in which the reduction of the Cu^{2+} ions occurred due to the decrease in the bond distance between the Cu^{2+} ions and the N in the $[Cu(En)_2]^{2+}$ complex, which enabled the electron transfer from N to Cu^{2+}.[23]

Calculation results

The equilibrium form of a crystal is defined by the free energies of its faces. Thus, by the Wulff construction principle and the theoretical values of the surface energy E_{surf},[41] obtained in a fixed volume, it is possible to predict the different morphologies that a material can possess.[1] Starting from an ideal morphology, and assuming that the crystal morphology is controlled by the lower-energy faces, which are the most stable, a map of the possible morphologies is obtained by adjusting the E_{surf} of the different faces. Subsequently, a comparison between theoretical and experimental morphologies, obtained using FE-SEM images, can be realized.[48]

In the case of α-Ag_2WO_4, consistent with the Wulff construction principle and the surface energy previously reported,[24] the experimental FE-SEM images obtained in this work resemble their respective theoretically predicted morphologies, as shown in Scheme 4. Initially, the ideal morphology is a prism dominated by surfaces (010), (100), and (001). During the synthesis, morphology A (see the inset in Scheme 4) is obtained by increasing the E_{surf} of face (001) to 0.80 J m^{-2}. When the energies of faces (110) and (011) are decreased to 0.20 and 0.68 J m^{-2}, respectively, morphology B (see inset in Scheme 4) is obtained. The C and D (Scheme 4) morphologies demonstrate the stabilization of face (011) by decreasing E_{surf} from 0.68 to 0.62 and 0.57 J m^{-2}, which corresponds to the WE0.5 sample. The images illustrate the evolution of the stabilization of faces (110) and (011) over the synthesis time from 0 to 32 min, resulting in the final morphology of the WE0.5 sample, which contains faces (110), (011), and (010).

A pathway connecting the ideal morphology with pathways displaying excellent agreement with the experimental morphologies was calculated and is depicted in Scheme 5. The polyhedron energy (E_{poly}) calculated from eqn (1) for the selected morphology of α-Ag_2WO_4 is summarized in Table 3. The energy profile was calculated by decreasing and/or increasing the E_{surf} values of a given surface of the polyhedron. An analysis of the energy profile shows a four-step process in which the first step is achieved by increasing the E_{surf} of face (001) and favors the appearance of face (101), obtaining the intermediate A shape. A subsequent decrease in the E_{surf} value for (110) and (011), which induces the formation of the B shape, predominantly exposes the (010) and (110) surface planes as well as the (011) surface plane. Finally, the decrease in E_{surf} for (011) leads to the final C and

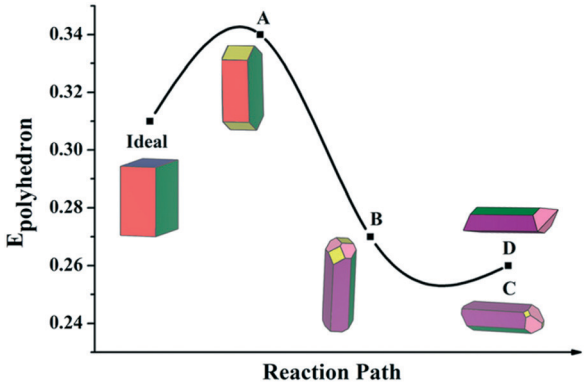

Scheme 5 Schematic representation of the energy profile to obtain the WE0.5 morphology. The intermediate morphologies are indicated as A–D, obtained by variations of the E_{surf} values.

D shapes (Scheme 5). It is important to note that both theoretical morphologies labelled C and D herein correspond to a minimum in the reaction coordinate diagram depicted in Scheme 5, indicating that the reaction path is thermodynamically favorable. This procedure can be considered an effective tool to investigate the morphology transformation and crystal growth mechanisms from a thermodynamic and kinetic point of view.[24]

Photoluminescence properties

These measurements were performed in order to investigate the influence of structural ordering and defects on the electronic energy level behavior. Fig. 8 shows the PL spectra of samples W, WE0.25, and WE0.5 at room temperature. The PL emission spectra of Ag_2WO_4 are generally deconvolved into two components, positioned in the blue- and green-light regions.[15] The PL spectra of the W and WE0.25 samples present a broadband profile in the visible spectral region with maximum emissions at 472 nm and 462 nm, respectively. The WE0.5 sample shows emission in the visible region between 400 nm and 650 nm with a maximum emission at 449 nm. The observed blue effect suggests that En causes distortions in the $[WO_6]$ clusters, as already discussed in Scheme 2, so the greater blue shift in the WE0.5 sample may be associated with the use of a higher concentration of the complexant.[21] These broadband profiles suggest that the emission involves electronic transitions from additional energy states within the band gap, also known as multiphononic and multilevel processes, whose origins are due to the distortions and defects of the $[AgO_y]$ (y = 2, 4, 6, and 7) and $[WO_6]$ clusters.[3] These distortions and defects generate a high density of intermediate energy states between valence and conduction bands with a slight energy variation from each other. The excited electrons transit through these energy levels for relaxation of the electron momentum through several pathways, thus emitting phonons to the lattice for later emission of photons in a wide energy range.

The PL spectra of the W and WE0.25 samples (Fig. 8(a–b)) were deconvoluted using three Gaussian functions at emission peaks centered at 448 nm (2.76 eV), 514 nm (2.41 eV), and 644 nm (1.93 eV). The spectrum of the WE0.5 sample (Fig. 8(c)) was deconvoluted with four emission peaks centered at 425 nm (2.92 eV), 449 nm (2.76 eV), 475 nm (2.61 eV), and 534 nm (2.32 eV). The pie charts (see insets in Fig. 8(a–c)) show the contribution percentage of each spectral region color. Emissions in the blue and green regions are due to the presence of distorted clusters, which produce more energetic emissions, 3.26–2.19 eV. Emissions in the red region are due to silver output and oxygen vacancies in the $[AgO_y]$ and $[WO_6]$ clusters, which in turn produce less energetic emissions, 2.19–1.59 eV.[21] Emissions in higher energetic regions are caused by structural defects in the crystalline lattice or shallow defects, because they give rise to energy levels close to the valence band (VB) and conduction band (CB). Emissions on the low energy side are known as deep defects, because they cause energy levels closer to the center of the band gap.[52]

It was observed that the higher concentration of En complexing agent added to the synthesis results in a larger amount of structural defects being introduced. As can be seen in the pie charts included in Fig. 8(a–c), the contribution of the oxygen vacancy defects goes from 55% to 39% to 0% for samples W, WE0.25, and WE0.5, respectively, whereas structural defects present in the material increased from 45% to 61% to 100% for W, WE0.25, and WE0.5 samples, respectively. These results corroborate the results of XPS, through which there is a decrease in oxygen vacancies in the sense of increasing the concentration of En employed. A possible explanation for the increase in structural defects is the reduction reaction of the Ag^+ ion caused by En. It was observed that the En complexing agent favoured the formation of metallic Ag, and may have contributed to the increase in the distortions of the lattice forming distorted $[WO_6]$ clusters of the WE0.5 sample, resulting in more disorder in the medium range. Therefore, the PL spectra confirm the oxygen vacancy disorders and structural defects for samples W and WE0.25, and structural defects for the WE0.5 sample due to the higher concentration of En.

Table 3 Surface energy values (E_{surf}, J m^{-2}), the contribution of the surface area by the total area (C_i, %), and the polyhedron energy (E_{poly}, J m^{-2}) of each intermediate morphology to obtain the WE0.5 sample (α-Ag_2WO_4)

E_{surf} (C_i,%)					
Surface	α-Ag_2WO_4 (ideal)	A	B	C	D
(010)	0.20(52.5)	0.20(56.0)	0.20(21.0)	0.20(20.3)	0.20(19.4)
(100)	0.38(27.6)	0.38(25.0)	0.38(0.00)	0.38(0.00)	0.38(0.00)
(001)	0.53(19.9)	0.80(0.00)	0.80(0.00)	0.80(0.00)	0.80(0.00)
(110)	0.65(0.00)	0.65(0.00)	0.20(64.5)	0.20(65.7)	0.20(64.3)
(101)	0.68(0.00)	0.68(19.0)	0.68(6.49)	0.68(0.15)	0.68(0.00)
(011)	0.83(0.00)	0.83(0.00)	0.68(8.00)	0.62(13.8)	0.57(16.3)
$E_{polyhedron}$	0.31	0.34	0.27	0.26	0.26

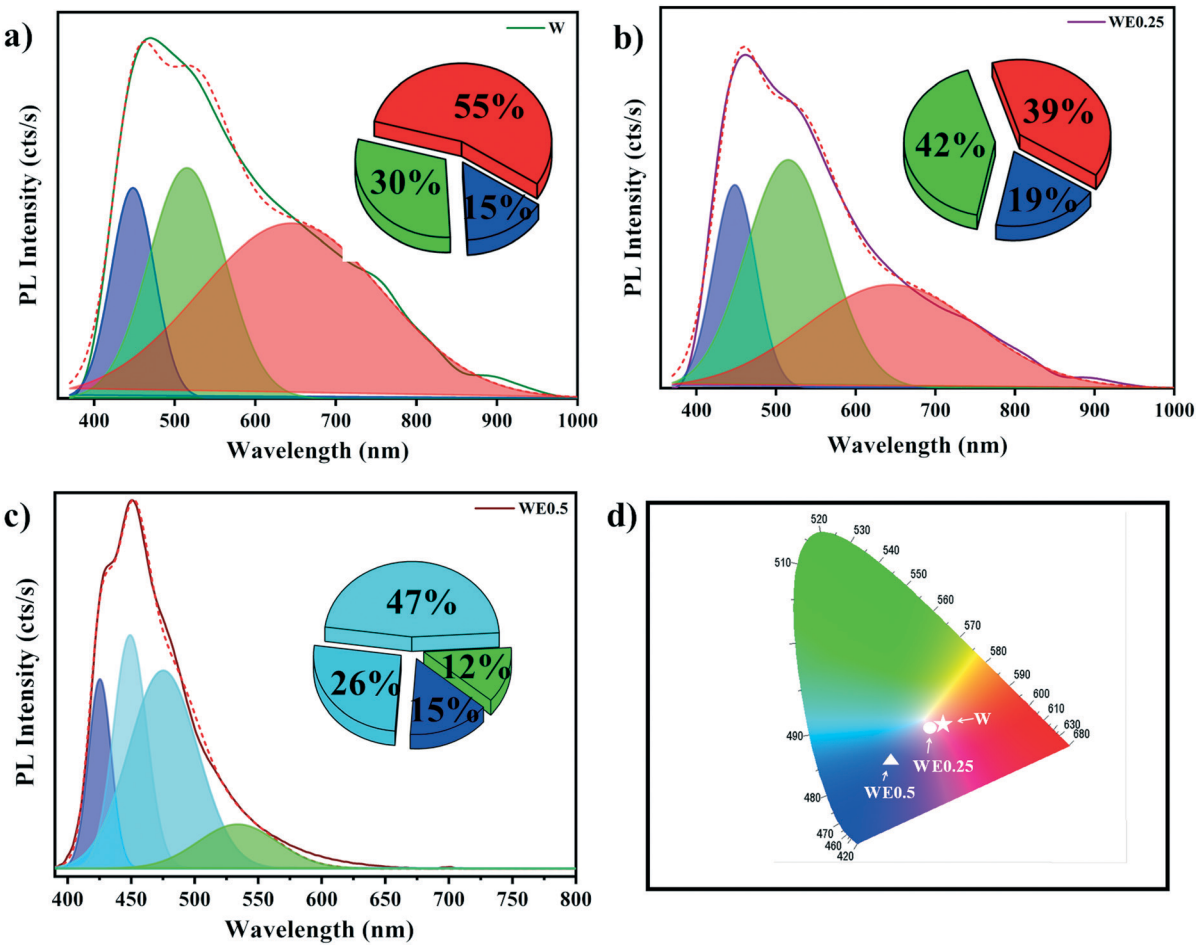

Fig. 8 Deconvolution of PL spectra. (Insets) The percentage of the color area corresponds to the emission peak of microcrystals a) W, b) WE0.25, c) WE0.5 and d) the CIE chromaticity diagram of α-Ag_2WO_4 samples.

The global PL emission of the samples is presented in the Diagram of the Commission International de L'Eclairage (CIE), chromaticity included, as shown in Fig. 8(d). The W sample presents emissions in the purplish pink color region with chromaticity coordinates x = 0.40 and y = 0.32, according to the literature.[52] The samples obtained with the En complexing agent showed a remarkable displacement in the emission color. For example: the WE0.25 sample with chromaticity coordinates x = 0.37 and y = 0.32 presents an emission near the white region, with approximately 40% structural defects and 60% vacancy defects. The WE0.5 sample, which presented a 100% structural defect contribution, showed chromaticity coordinates at x = 0.25 and y = 0.23, with an emission in the blue region. Thus, the concentration of En significantly modified the overall PL emission of the samples. The NPs that were deposited on the surface constitute plasmon NPs. These surface plasmons involve electron motion in the metal, which allows light to be concentrated in nanometer-scale volumes or hot spots. This physics effect can lead to enhanced light–matter interactions at the PL.

Knowing that ethylenediamine disorganizes tungstate clusters, it is possible to model the synthesis methodology to obtain other tungstates that emit in specific regions, such as, for example, white, controlling the disorder of the forming clusters, the network modifiers and the emission intensity, with the purpose of using these materials in LEDs.

Photocatalytic performance

The photocatalytic activity of the as-obtained samples was also analyzed, noting that the WE0.25 and WE0.5 samples showed low potential for photodegradation compared to sample W, as presented in Fig. 9(a and b). This behavior can be caused by two effects: 1) excess metallic Ag on the surface, and 2) reduction of oxygen vacancies in the material structure.

The amount of Ag metallic particles on the surface of α-Ag_2WO_4 followed the inverse order of photocatalytic activity W < WE0.25 < WE0.5. These results corroborate the investigation reported by Liu *et al.*[22] who synthesized Ag/α-Ag_2WO_4 utilizing the CH method, followed by the chemical reduction process.

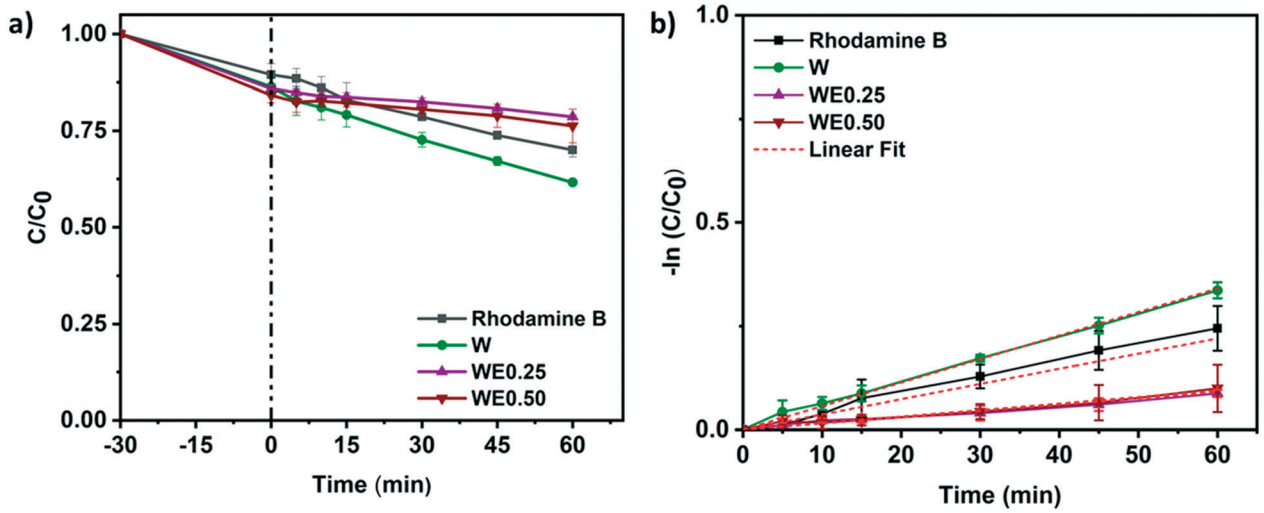

Fig. 9 a) Photocatalytic activities of samples in degradation of RhB under ultra-violet light irradiation, and b) corresponding plot of $-\ln(C/C_0)$ *versus* time.

These researchers observed that the samples which presented excess Ag metallic particles on the surface exhibited low photoactivity compared to the samples with a suitable amount of silver. The authors linked this phenomenon with the fact that the excess silver covers the surface available for the photochemical reaction and hinders the transfer of electrons to the outside, reducing the photocatalytic activity.

It is interesting to note that, although the samples obtained by Liu *et al.* are decorated with silver, their proportion is not detected by XRD. The samples obtained by this work, on the other hand, present two well-defined phases of α-Ag_2WO_4 and metallic Ag identified by XRD. Therefore, the proportion, as already estimated in the refinement calculations, is much higher than that obtained by Liu *et al.* As already mentioned, the excess of superficial silver hindered the performance of the samples.

In our work, the density of oxygen vacancies followed the direct order of the photocatalytic activity WE0.5 < WE0.25 < W. Different literature reports describe the photochemical reaction mechanism presented in this work, as shown in eqn (6)–(10).[24,53] In this mechanism, the radical cluster $[AO_z]^{\bullet}$ interacts with water, producing, among other things, the hydroxyl radical, OH*, which is extremely oxidizing (eqn (8)). Meanwhile, electrons $[AO_z]'$ react with O_2 producing O_2' which, when interacting with the $H^{\bullet}$ species, produces the peroxide radical HO_2^* (see eqn (7) and (9)). As previously discussed, the PL graphs in Fig. 8 showed that the complexing agent hindered the participation of oxygen vacancies in electronic transitions; therefore, the production of hydroxyl radicals is reduced in the WE0.25 sample and virtually eliminated in the WE0.5 sample. However, the reaction of electrons with O_2 still occurs, leading to the minor photocatalytic activity of the material, and the low effectiveness due to metallic Ag, which prevents the transfer of electrons to the outside, making them unavailable for the photocatalytic reaction.

$$[AO_z]^x + [AO_{z-1}V_0]^x \rightarrow [AO_z]' + [AO_z]^{\bullet} \quad (6)$$

$$[AO_z]' + O_2 \rightarrow [AO_z]^x + O_2' \quad (7)$$

$$[AO_z]^{\bullet} + H_2O \rightarrow [AO_z]^x + OH^* + H^{\bullet} \quad (8)$$

$$O_2' + H^{\bullet} \rightarrow HO_2^* \quad (9)$$

$$HO_2^* + OH^* + OC \rightarrow CO_2 + H_2O + COC \quad (10)$$

When A = W, z = 6 or A = Ag, z = 2, 4, 6 or 7.

OC = organic compounds and COC = colorless organic compounds.

It is also possible to adjust the proportion of ethylenediamine used in the synthesis, to obtain Ag/Ag_2WO_4 with better photocatalytic performance.

Conclusions

In conclusion, Ag/α-Ag_2WO_4 was successfully obtained *via* the MAH method. For the first time, the ethylenediamine (En) complexing agent was used to control the morphological characteristics, structural order/disorder, optical properties, and photocatalytic performance of α-Ag_2WO_4 crystals. En also reduced Ag^+ in the synthesis process proposed in this work, playing a fundamental role in the decoration of Ag NPs. Also observed was a favorable emission near the white light (WE0.25) and blue light (WE0.5) regions. The photocatalytic tests confirmed that the excess surface metallic silver and the removal of oxygen vacancies were essential for a good photocatalytic performance of α-Ag_2WO_4. Our investigation showed that En can modulate the structural, morphological, and optical properties of α-Ag_2WO_4, and also decorate it with Ag NPs. This semiconductor framework represents a promising alternative to metals, as its plasmon frequency can

be controlled in the crystal formation step by blocking certain positions of the primary clusters. Therefore, it represents a type of tunable, high-quality material for plasmonic applications. Finally, the growth mechanism of the particles, which results in interesting multidimensional structures, together with the decoration of Ag NPs, indicates the possibility of obtaining structures with modeled optical and photocatalytic properties, by controlling the concentration of the complexing agent.

Funding sources

We acknowledge the financial support of the following Brazilian research funding institutions: CNPq (443733/2018-0), FAPESP-CDMF (2013/07296-2, and 2017/12437-5), and CAPES (Finance Code 001).

Conflicts of interest

The authors declare that they have no conflict of interest.

Acknowledgements

This research was partially performed at the LNLS (project XAFS2-20180338), Campinas, SP, Brazil. We acknowledge the financial support of the following Brazilian research funding institutions: CNPq (443733/2018-0), FAPESP-CDMF (2013/07296-2, and 2017/12437-5), and CAPES (Finance Code 001). The authors are grateful to Mr. Rorivaldo De Camargo for operating the FE-SEM and HR-TEM equipment, and Dr. Francisco N. Souza Neto, Mrs. Daniela Caceta, Ms. Luma Garcia, and Mrs. Sandra Bellini for all the support provided for the development of this work.

References

1 J. Andrés, L. Gracia, A. F. Gouveia, M. M. Ferrer and E. Longo, *Nanotechnology*, 2015, **26**, 405703.
2 Y. Bi, H. Hu, S. Ouyang, G. Lu, J. Cao and J. Ye, *Chem. Commun.*, 2012, **48**, 3748–3750.
3 M. D. P. Silva, R. F. Gonçalves, I. C. Nogueira, V. M. Longo, L. Mondoni, M. G. Moron, Y. V. Santana and E. Longo, *Spectrochim. Acta, Part A*, 2016, **153**, 428–435.
4 J. L. Cerrillo, A. E. Palomares and F. Rey, *Microporous Mesoporous Mater.*, 2020, **305**, 110367.
5 M. Asghar, S. Habib, W. Zaman, S. Hussain, H. Ali and S. Saqib, *Microsc. Res. Tech.*, 2020, 1–12.
6 X. Xin, Y. Gao, Q. Zhang, Z. Wang, D. Sun, S. Yuan and H. Xia, *Soft Matter*, 2018, **14**, 8352–8360.
7 A. Koyappayil, S. Berchmans and M. H. Lee, *Colloids Surf., B*, 2020, **189**, 110840.
8 D. Liu, W. Huang, L. Li, L. Liu, X. Sun, B. Liu, B. Yang and C. Guo, *Nanotechnology*, 2012, **28**, 1–10.
9 K. Dai, J. Lv, L. Lu, C. Liang, L. Geng and G. Zhu, *Mater. Chem. Phys.*, 2016, **177**, 529–537.
10 S. Li, W. Jiang, S. Hu, Y. Liu and J. Liu, *Mater. Lett.*, 2018, **224**, 29–32.
11 D. Xu, B. Cheng, J. Zhang, W. Wang, J. Yu and W. Ho, *J. Mater. Chem. A*, 2015, **3**, 20153–20166.
12 D. Barreca, A. Gasparotto, C. Maragno, E. Tondello and S. Gialanella, *J. Appl. Phys.*, 2005, **97**, 054311.
13 D. Barreca, A. Gasparotto, C. Maragno, E. Tondello and S. Gialanella, *J. Nanosci. Nanotechnol.*, 2007, **7**, 2480–2486.
14 L. F. Da Silva, A. C. Catto, W. Avansi, L. S. Cavalcante, J. Andrés, K. Aguir, V. R. Mastelaro and E. Longo, *Nanoscale*, 2014, **6**, 4058–4062.
15 L. S. Cavalcante, M. A. P. Almeida, W. Avansi, R. L. Tranquilin, E. Longo, N. C. Batista, V. R. Mastelaro and M. S. Li, *Inorg. Chem.*, 2012, **51**, 10675–10687.
16 A. Sreedevi, K. P. Priyanka, S. C. Vattappalam and T. Varghese, *J. Electron. Mater.*, 2018, **47**, 6328–6333.
17 A. Sreedevi, K. P. Priyanka, K. K. Babitha, N. Aloysius Sabu, T. S. Anu and T. Varghese, *Indian J. Phys.*, 2015, **89**, 889–897.
18 C. H. B. Ng and W. Y. Fan, *CrystEngComm*, 2016, **18**, 8010–8019.
19 F. X. Nobre, I. S. Bastos, R. O. dos Santos Fontenelle, E. A. A. Júnior, M. L. Takeno, L. Manzato, J. M. E. de Matos, P. P. Orlandi, J. de Fátima Souza Mendes, W. R. Brito and P. R. da Costa Couceiro, *Ultrason. Sonochem.*, 2019, **58**, 104620.
20 Y. Lu, Y. J. Deng, X. Y. Zhang and J. K. Liu, *Mater. Technol.*, 2017, **32**, 178–185.
21 E. Longo, D. P. Volanti, V. M. Longo, L. Gracia, I. C. Nogueira, M. A. P. Almeida, A. N. Pinheiro, M. M. Ferrer, L. S. Cavalcante and J. Andrés, *J. Phys. Chem. C*, 2014, **118**, 1229–1239.
22 D. Liu, W. Huang, L. Li, L. Liu, X. Sun, B. Liu, B. Yang and C. Guo, *Nanotechnology*, 2017, **28**, 1–10.
23 X. Wang, K. Han, F. Wan, Y. Gao and K. Jiang, *Mater. Lett.*, 2008, **62**, 3509–3511.
24 N. G. Macedo, A. F. Gouveia, R. A. Roca, M. Assis, L. Gracia, J. Andrés, E. R. Leite and E. Longo, *J. Phys. Chem. C*, 2018, **122**, 8667–8679.
25 H. M. Rietveld, *J. Appl. Crystallogr.*, 1969, **2**, 65–71.
26 L. W. Finger, D. E. Cox and A. P. Jephcoat, *J. Appl. Crystallogr.*, 1994, **27**, 892–900.
27 P. W. Stephens, *J. Appl. Crystallogr.*, 1999, **32**, 281–289.
28 R. J. Hill and C. J. Howard, *J. Appl. Crystallogr.*, 1987, **20**, 467–474.
29 H. M. Rietveld, *Acta Crystallogr.*, 1967, **22**, 151–152.
30 P. M. Skarstad and S. Geller, *Mater. Res. Bull.*, 1975, **10**, 791–799.
31 R. Becherer and G. Ifland, *Naturwissenschaften*, 1954, **4**, 471.
32 M. Alain, M. Jacques, M. B. Diane and P. Karine, *J. Phys.: Conf. Ser.*, 2009, **190**, 012034.
33 D. Stone, J. Liu, D. P. Singh, C. Muratore, A. A. Voevodin, S. Mishra, C. Rebholz, Q. Ge and S. M. Aouadi, *Scr. Mater.*, 2010, **62**, 735–738.
34 P. Demokritou, R. Bchel, R. M. Molina, G. M. Deloid, J. D. Brain and S. E. Pratsinis, *Inhalation Toxicol.*, 2010, **22**, 107–116.
35 K. Momma and F. Izumi, *J. Appl. Crystallogr.*, 2008, **41**, 653–658.
36 C. Hu, Y. Lan, J. Qu, X. Hu and A. Wang, *J. Phys. Chem. B*, 2006, **110**, 4066–4072.

37 D. Chen, Y. Zhang, T. Bessho, J. Sang, H. Hirahara, K. Mori and Z. Kang, *Chem. Eng. J.*, 2016, **303**, 100–108.
38 J. Lv, K. Dai, J. Zhang, L. Lu, C. Liang, L. Geng, Z. Wang, G. Yuan and G. Zhu, *Appl. Surf. Sci.*, 2017, **391**, 507–515.
39 M. Pirhashemi and A. Habibi-Yangjeh, *J. Colloid Interface Sci.*, 2017, **491**, 216–229.
40 M. Blais-Roberge, M. Rioux, Y. Ledemi and Y. Messaddeq, *J. Non-Cryst. Solids*, 2017, **470**, 61–69.
41 F. Y. Xie, L. Gong, X. Liu, Y. T. Tao, W. H. Zhang, S. H. Chen, H. Meng and J. Chen, *J. Electron Spectrosc. Relat. Phenom.*, 2012, **185**, 112–118.
42 G. Poirier, F. C. Cassanjes, Y. Messaddeq, S. J. L. Ribeiro, A. Michalowicz and M. Poulain, *J. Non-Cryst. Solids*, 2005, **351**, 3644–3648.
43 R. V. Vedrinskii, V. L. Kraizman, A. A. Novakovich, P. V. Demekhin and S. V. Urazhdin, *J. Phys.: Condens. Matter*, 1998, **10**, 9561–9580.
44 A. Kuzmin and J. Purans, *Radiat. Meas.*, 2001, **33**, 583–586.
45 S. Yamazoe, Y. Hitomi, T. Shishido and T. Tanaka, *J. Phys. Chem. C*, 2008, **112**, 6869–6879.
46 S. K. Gupta, K. Sudarshan, P. S. Ghosh, S. Mukherjee and R. M. Kadam, *J. Phys. Chem. C*, 2016, **120**, 7265–7276.
47 A. Turkovic, L. Fox, J. F. Scott, S. Geller and G. F. Ruse, *Mater. Res. Bull.*, 1977, **12**, 189–196.
48 V. M. Longo, C. C. De Foggi, M. M. Ferrer, A. F. Gouveia, R. S. André, W. Avansi, C. E. Vergani, A. L. Machado, J. Andrés, L. S. Cavalcante, A. C. Hernandes and E. Longo, *J. Phys. Chem. A*, 2014, **118**, 5769–5778.
49 H. Feilchenfeld and O. Siiman, *J. Phys. Chem.*, 1986, **90**, 4590–4599.
50 J. Ding, X. Liu, M. Wang, Q. Liu, T. Sun, G. Jiang and Y. Tang, *CrystEngComm*, 2018, **20**, 4499–4505.
51 Z. Wang and R. Yu, *Adv. Mater.*, 2019, **31**, 1–34.
52 M. Mondego, R. C. de Oliveira, M. Penha, M. S. Li and E. Longo, *Ceram. Int.*, 2017, **43**, 5759–5766.
53 L. S. Cavalcante, J. C. Sczancoski, N. C. Batista, E. Longo, J. A. Varela and M. O. Orlandi, *Adv. Powder Technol.*, 2013, **24**, 344–353.